

A systematic construction of Gaussian basis sets for the description of laser field ionization and high-harmonic generation

Aleksander P. Woźniak,^{1,*} Michał Lesiuk,¹ Dmitry K. Efimov,² Michał Mandrysz,² Jakub S. Prauzner-Bechcicki,³ Marcelo Ciappina,⁴ Emilio Pisanty,⁴ Jakub Zakrzewski,^{5,6} Maciej Lewenstein,^{4,7} and Robert Moszyński¹

¹*Faculty of Chemistry, University of Warsaw, Pasteura 1, 02-093 Warsaw, Poland*

²*Institute of Theoretical Physics, Jagiellonian University in Krakow, Łojasiewicza 11, 30-348 Kraków, Poland*

³*Marian Smoluchowski Institute of Physics, Jagiellonian University in Krakow, Łojasiewicza 11, 30-348 Kraków, Poland*

⁴*ICFO - Institut de Ciències Fotoniques, The Barcelona Institute of Science and Technology, Av. Carl Friedrich Gauss 3, 08860 Castelldefels (Barcelona), Spain*

⁵*Institute of Theoretical Physics, Jagiellonian University in Krakow, Łojasiewicza 11, 30-348 Kraków, Poland*

⁶*Mark Kac Complex Systems Research Center, Jagiellonian University in Krakow, Łojasiewicza 11, 30-348 Kraków, Poland*

⁷*ICREA, Pg. Lluís Companys 23, 08010 Barcelona, Spain*

(Dated: July 28, 2020)

A precise understanding of mechanisms governing the dynamics of electrons in atoms and molecules subjected to intense laser fields has a key meaning for the description of phenomena such as the high-harmonic generation and ionization. From the theoretical point of view this is still a challenging task, as the currently existing methods of solving the time-dependent Schrödinger equation are characterized with either limited accuracy, or limited applicability. In this paper we explore the method of expanding the wavefunction of the examined system into a linear combination of atom-centered basis functions, and present a novel systematic scheme for constructing an optimal Gaussian basis set suitable for the description of excited and continuum atomic or molecular states. We analyze the performance of the proposed basis sets by performing a series of time-dependent configuration interaction calculations for the hydrogen atom in fields of intensity varying from 5×10^{13} W/cm² to 5×10^{14} W/cm². We also compare the results with data obtained using Gaussian basis sets proposed previously by other authors.

PACS numbers: 42.65.Ky, 32.80.Rm

I. INTRODUCTION

Attoscience is a rapidly developing area of research with opportunities of unprecedented applications in physics, chemistry and biology. In attoscience, the basic process consist of shining a short (a few optical cycles long) pulse of near- or mid-infrared laser radiation on a target, which can be an atom, a molecule, a biomolecule, etc [1–3]. The response of the target may result in high-harmonic generation (HHG) [4–11] and, if the intensity of the pulse is high enough, in electron detachment and formation of atomic or molecular ions [12–30]. The high harmonics are generated as a part of a macroscopic, phase-matched process [31], and manifest themselves as XUV or X-ray pulses at frequencies given by integer multiples of the driving pulse frequency [32–36]. These pulses are not very intense, but they have attosecond-scale duration, and exhibit a very high spatial and temporal coherence [37–40], so they allow for imaging of the structure and dynamics of matter in its natural length and time scales.

The HHG spectrum is characterized by its distinctive shape. For a few lowest harmonic peaks, the intensity decreases with the harmonic order according to lowest-order perturbation theory [41]. Afterwards, a long plateau is observed in which the harmonic peaks are of a similar height. This plateau terminates with a sharp cutoff,

beyond which the emission decays exponentially. This shape is usually explained using a semiclassical picture, encoded in the famous three-step model of HHG [7–9]. In the first step, the electron escapes the potential well of the nucleus via tunneling ionization. In the second step, it is further accelerated in the laser field until the direction of the field changes. Finally, in the third step, it is reaccelerated toward the residual ion and recombines with it, which is accompanied by an emission of a high-energy photon. The maximum energy of the emitted photons, and thus the position of the harmonic cutoff, depends on the ponderomotive energy U_p and on the ionization potential I_p via the relation $E_{\text{cutoff}} = I_p + 3.17U_p$. For inversion-symmetric media, such as atoms in the gas phase, only peaks at odd harmonics are present in the spectrum, due to symmetry constraints.

Theoretical description of the HHG spectra requires the knowledge of the time evolution of the dipole moment in the non-perturbative regime. This is a formidable task, since it in turn requires solving the time-dependent Schrödinger equation (TDSE) [42]. This problem can be treated in two ways: either by diverse analytical methods or by solving the TDSE using a variety of numerical methods [43]. In the former case, the strong field approximation (SFA) is undoubtedly the method of choice. SFA is the first step in getting a basic understanding of HHG and related phenomena in various new settings [9, 42, 44–46]. Indeed, SFA provides an intuitive basis for interpretation of the numerical solutions of TDSE and,

* awozniak@chem.uw.edu.pl

for example, allows for decoding information about the target atom, molecule or solid from the high-harmonic spectra [47, 48]. In the case of numerical techniques for solving the TDSE, recent developments in real-time propagation of the wavefunction on a finite spatial grid have proven extremely useful for the description and understanding of the electron dynamics during processes such as the high-harmonic generation and ionization [49–63]. However, the explicit full-dimensional numerical integration of TDSE is applicable mostly to one-electron systems, such as the hydrogen-like ions and the H_2^+ ion, and the extension to two-electron systems, such as the helium atom, remains a great challenge [64–71]. Extending this approach to more complex systems is barely feasible, as it requires huge amounts of memory and computational time, and must rely on using various approximations, such as the most commonly used single-active-electron approximation [6, 72–83]. Such techniques have some serious limitations, as pointed out e.g. by Gordon *et al.* [84]. To go beyond the single-active-electron approximation one may resort to restricted dimensionality models [85–96] - an approach that yields accurate predictions of many strong-field phenomena including the study of spin-dependent effects in three-electron systems [97–100]. Nevertheless, the results obtained with these methods are qualitative in nature and the formalism is difficult to extend to many-electron systems like molecules. Still, a valuable insight into the strong-field phenomena, especially in the context of many-electron systems or interactions with elliptically polarized laser pulses, is gained from a classical and semiclassical analysis [101–110]. However, when it comes to the reproduction of the high-harmonic spectra the classical methods alone turn out to be too complicated [111]. Due to the limitations discussed, novel methods that can describe many-electron systems are still in high demand.

A remedy for this problem may be to apply the methods that are widely used in quantum chemistry. In general, they employ the expansion of the wavefunction of the examined system into a linear combination of predefined, atom-centered square-integrable L^2 functions that imitate the atomic orbitals, called the basis set. Currently, for a majority of the widely-used quantum chemistry methods real-time time-dependent counterparts have been developed and applied to the real-time propagation, including time-dependent Hartree-Fock [112–117], time-dependent configuration interaction [118–124], time-dependent density functional theory [117, 125–128], algebraic diagrammatic construction [129, 130], and time-dependent coupled cluster [131–133]. The basis set approach is much less limited by the number of electrons and atoms than the grid-based approach. It is also computationally less expensive, since most of the necessary calculations can be performed analytically. The most common type of functions used in quantum chemistry are the so-called Gaussian-type or-

bitals (GTOs) of general (normalized) form

$$\chi_{lm;\alpha}^{\text{GTO}}(r, \theta, \phi) = \sqrt{\frac{2(2\alpha)^{l+3/2}}{\Gamma(l + \frac{3}{2})}} r^l \exp(-\alpha r^2) Y_{lm}(\theta, \phi). \quad (1)$$

where $Y_{lm}(\theta, \phi)$ are the spherical harmonics and α is a positive real number. The GTOs have some particularly convenient mathematical properties that allow for a fast and efficient computation of many-center integrals, required in calculations for polyatomic molecules. Nowadays the calculations using GTO basis sets are routinely performed for systems containing thousands of electrons. However, since most of quantum chemical studies are focused on determining the properties of atoms and molecules in their ground states, a great majority of the existing atomic basis sets, such as Pople, Dunning or Ahlrichs basis sets, have been obtained by minimizing the atomic ground state energies at a suitable level of theory (usually the Hartree-Fock or a simple post-HF method) [134]. It is thus natural that these basis sets approximate the lowest energy states much more accurately than the excited states. During a real-time propagation, the atoms or molecules in intense laser fields usually become excited to states near or above the ionization threshold. What we need, then, are basis sets which are able to describe a sufficiently large number of excited and continuum atomic or molecular states, with a precision comparable to that of the description of the ground state.

It is quite obvious that the construction of a Gaussian basis that correctly mimics the oscillatory behavior of the continuum orbitals is far from trivial. Fiori and Miraglia [135] and later Szczygieł *et al.* [136] introduced a new approach for approximating the continuum wave functions of the hydrogen atom with a square integrable basis set to describe the ionization processes. This basis set consists of plane wave functions multiplied by the Gaussian type orbitals (GTOPWs or London orbitals), which mimic the oscillatory behavior of the continuum orbital. It turned out that with this basis set one could very accurately reproduce the measured ionization spectra of the hydrogen and helium atoms as well as molecular-frame photoelectron angular distributions for the hydrogen molecule [135, 136]. However, this approach failed to exceed beyond the perturbative regime.

One of the very first concepts of a pure Gaussian basis set designed specifically for the description of the Rydberg and continuum molecular states was conceived by Kauffman *et al.* in 1989 [137]. They presented a method for constructing a set of Gaussian-type orbitals (GTOs) with the exponents fitted to maximize their overlaps with a series of the so-called Slater-type orbitals (STOs)

$$\chi_{nlm;\zeta}^{\text{STO}}(r, \theta, \phi) = \frac{(2\zeta)^{n+1/2}}{\sqrt{\Gamma(2n+1)}} r^{n-1} \exp(-\zeta r) Y_{lm}(\theta, \phi) \quad (2)$$

with a constant exponent ζ and a variable positive integer principal quantum number n . In principle, the idea

behind this is appealing, because STOs constitute a complete basis set in the Hilbert space, making it possible to describe the electronic continuum without the need to use any non-square-integrable functions. Kaufmann has shown that his functions (referred to as the Kaufmann functions or K functions further in the text) are able to generate a discretized spectrum of the continuum eigenfunctions and imitate the Coulomb wave functions up to considerably long distances away from the nuclei [137].

Unfortunately, the Kaufmann functions also possess some major drawbacks. First, since each STO is described with a single GTO, the size of the basis set scales linearly with the number of STOs to be reproduced. Moreover, the high- n STOs are approximated less accurately compared to the low- n ones. Finally, the STOs form a non-orthogonal basis set, and the overlap integral between two adjacent STOs approaches unity with increasing n . It therefore follows that, for large n , the values the exponents of the K functions also become closer to each other, creating a risk of linear dependencies appearing in the basis set, which may jeopardize the numerical stability of the calculations.

The disadvantages listed above make the Kaufmann basis sets rather ineffective for the description of states close to or beyond the ionization threshold, the description of which may require including STOs with very high principal quantum numbers. Therefore, their applicability in attoscience is limited to simulating atoms and molecules in laser fields of relatively low intensities. Due to the same reason, the K functions may be inefficient for the description of heavier elements. Since the STO's principal quantum number can be associated with the atomic shell number, for atoms with a large number of occupied shells it may turn out that the linear dependencies and fitting inaccuracies prevent one from representing more than a few lowest excited states accurately.

It is worth noting that after the publication of the paper by Kaufmann *et al.* several attempts to create Gaussian basis sets suitable for the description of the excited and continuum states have appeared. Nestmann and Peyerimhoff reported fitting linear combinations of GTOs to spherical Bessel functions for the purpose of the electron-molecule scattering calculations [138]. Their work was later extended to the Coulomb wave functions by Faure *et al.* [139]. Some more elaborate approaches, such as the B -spline basis sets or combinations of Gaussians and grid-based methods, have also been employed with success in describing both ionization rates and HHG [140–145].

Recently, Coccia and collaborators have decided to revisit and extend the work of Kaufmann *et al.* with the primary goal of constructing basis sets for an accurate description of atomic and molecular HHG spectra [145–150]. They combined the K functions with augmented Dunning basis sets containing a very large number of diffuse functions [151]. Their method proved useful for the description of HHG at intensities below the barrier-suppression ionization threshold. However, the limita-

tions stemming from the use of the K functions, such as near-linear dependencies within this basis set, could not be avoided.

In this paper we introduce a novel systematic scheme for constructing finite Gaussian basis sets for an optimal representation of both bound and continuum eigenstates of the Hamiltonian. Recalling the benefits of the Kaufmann approach, such as simplicity and physical interpretability of the K functions, we determine a series of Gaussian functions to best reproduce a given subset of STOs. However, our approach is somewhat different. Instead of optimizing a single GTO for each consecutive STO, we optimize all GTOs at the same time, so that every STO from a predefined range may be approximated by their linear combination with a roughly equal accuracy.

The paper is organized as follows. In Section II we briefly discuss the theory behind the basis set approach to real-time propagation. The procedure used to obtain optimal Gaussian basis sets is described in detail in Section III. The computational details are presented in Section IV. In Section V we present and discuss the results obtained via real-time propagation of the hydrogen atom wavefunction using constructed basis sets. We also compare them with the results obtained using basis sets composed of the K functions and using the grid-based approach. Finally, Section VI is a brief summary of this work.

II. OUTLINE OF THE THEORY

The main goal of the real-time propagation approach is to solve the time-dependent Schrödinger equation

$$i\frac{\partial}{\partial t}|\Psi(\mathbf{r}, t)\rangle = \hat{H}(t)|\Psi(\mathbf{r}, t)\rangle, \quad (3)$$

where both the Hamiltonian and the wavefunction depend explicitly on time. Most numerical approaches introduce the propagator derived from the Magnus expansion [152] which connects the wavefunctions at times t_1 and t_2 :

$$U(t_2, t_1) = \hat{T} \exp \left(-i \int_{t_1}^{t_2} \hat{H}(t) dt \right) \quad (4a)$$

$$|\Psi(\mathbf{r}, t_2)\rangle = U(t_2, t_1)|\Psi(\mathbf{r}, t_1)\rangle \quad (4b)$$

via a time-ordered matrix exponential. It is then assumed that the total evolution time can be divided into a large number of small yet finite timesteps Δt during which the time-dependency of the Hamiltonian can be ignored, and the integral formula for the propagator is replaced with a finite difference one:

$$U(t + \Delta t, t) = \exp(-i\Delta t H(t + \Delta t/2)). \quad (5)$$

The fractional timestep was introduced by using the midpoint rule when approximating the integral of the Hamiltonian from t to $t + \Delta t$.

When solving the TDSE using the grid-based methods, the real-time propagation may be performed by recalculating at each timestep the values of the wavefunction at the given set of points in space. However, there is also an alternative approach. In most cases the Hamiltonian can be expressed as a sum of a time-independent part H_0 , describing the unperturbed atom or molecule, and a time-dependent light-matter interaction operator $V(t)$, $\hat{H}(t) = \hat{H}_0 + \hat{V}(t)$. The unperturbed Hamiltonian is usually a Hermitian operator, so its eigenstates constitute a complete basis set in the Hilbert space. Therefore, the wavefunction at any time t may be expanded in this basis:

$$|\Psi(\mathbf{r}, t)\rangle = \sum_{n=1}^{\infty} c_n(t) |\psi_n(\mathbf{r})\rangle. \quad (6)$$

Thus, we reduce the problem of finding the time-dependent wavefunction to a much simpler problem of finding the time-dependent coefficients corresponding to time-independent Hamiltonian eigenstates. The remaining problem is how to obtain the necessary eigenstates. In most quantum chemistry methods, they are approximated by diagonalizing the (unperturbed) Hamiltonian matrix \mathbf{H}_0 in a predefined set of functions χ_k (the basis set), with the matrix elements $(H_0)_{mn} = \langle \chi_m | \hat{H}_0 | \chi_n \rangle$. The expression for the approximate time-dependent wavefunction expanded in the basis set then reads as follows

$$|\Psi(\mathbf{r}, t)\rangle = \sum_{n=1}^K c_n(t) \sum_{k=1}^K c_k \chi_k(\mathbf{r}) = \sum_{k=1}^K c'_k(t) \chi_k(\mathbf{r}). \quad (7)$$

We are now able to replace the wavefunction with a column matrix $\mathbf{c}(t)$ of the time-dependent coefficients $c'_k(t)$ and reformulate the propagation equation (4) with the propagator (5) as a matrix equation

$$\mathbf{c}(t + \Delta t) = \exp(-i\Delta t[\mathbf{H}_0 + \mathbf{V}(t + \Delta t/2)]) \mathbf{c}(t), \quad (8)$$

where the matrix $\mathbf{V}(t)$ is constructed analogously to the matrix \mathbf{H}_0 .

Note should also be taken on the possible mathematical form of the basis functions. In the single-electron case they are simply L^2 functions of three position variables, the linear combination of which approximates the hydrogen-like orbitals. This also applies for the time-dependent Hartree-Fock and time-dependent density functional theory methods, where the approximate eigenstates are the Hartree-Fock or Kohn-Sham orbitals. In the post-TDHF methods, such as time-dependent configuration interaction, the basis set comprises of the ground state and excited Slater determinants.

The two key observables obtained from the real-time propagation are the HHG spectrum and the ionization probability. In this paper the former is calculated in the dipole form, as the squared modulus of the Fourier transform of the z component of the time-resolved dipole mo-

ment:

$$I_{\text{HHG}}(\omega) = \left| \int_0^{t_f} \langle \Psi(\mathbf{r}, t) | d_z | \Psi(\mathbf{r}, t) \rangle e^{i\omega t} dt \right|^2. \quad (9)$$

In the basis set approach $\langle d_z \rangle$ is calculated from the following expression:

$$\langle \Psi(\mathbf{r}, t) | d_z | \Psi(\mathbf{r}, t) \rangle = \sum_{i=1}^K \sum_{j=1}^K [c'_i(t)]^\dagger c'_j(t) \langle \chi_i(\mathbf{r}) | d_z | \chi_j(\mathbf{r}) \rangle. \quad (10)$$

The ionization probability is calculated from the time-resolved norm of the wavefunction during the propagation with absorbing boundary conditions:

$$W(t) = 1 - \langle \Psi(\mathbf{r}, t) | \Psi(\mathbf{r}, t) \rangle. \quad (11)$$

III. BASIS SETS

The Slater-type orbitals are derived from the so-called Laguerre orbitals

$$\chi_{nlm;\zeta}^L(r, \theta, \phi) = (2\zeta)^{l+5/2} \sqrt{\frac{(n-l-1)!}{(n+l+1)!}} \times r^l L_{n-l-1}^{2l+2}(2\zeta r) \exp(-\zeta r) Y_{lm}(\theta, \phi) \quad (12)$$

where L_{n-l-1}^{2l+2} represents an associated Laguerre polynomial of degree $n-l-1$. The quantum numbers n , l , and m take on the same values as for the hydrogen atom solutions, i.e. $n \geq 1$, $l < n$ and $-l \leq m \leq l$. As opposed to the hydrogenic orbitals, the Laguerre orbitals constitute a complete orthonormal $L^2(\mathbb{R}^3)$ basis set, therefore they are suitable for the description of both bound and continuum molecular states. However, the polynomial structure of their radial functions makes them difficult to approximate with the commonly used Gaussian functions. The Laguerre orbitals can be simplified by retaining only the term of the highest power of r from the Laguerre polynomial, resulting in the Slater-type orbitals. Due to the loss of the nodal structure of their radial functions, the STOs are no longer orthogonal, but still constitute a complete basis set, as each Laguerre function can be expanded in terms of STOs [153].

From the perspective of real-time propagation, the Slater-type orbitals have some particularly useful properties: their radial functions are identical for all angular momenta, and they have an expectation value of r given by

$$\langle \chi_{nlm;\zeta}^{\text{STO}} | r | \chi_{nlm;\zeta}^{\text{STO}} \rangle = \frac{2n+1}{2\zeta}. \quad (13)$$

Since in the real-time-dependent methods the wavefunction is most often propagated in a finite region of space (usually accompanied by a complex absorbing potential or a mask function to eliminate reflections, as we will

elaborate in Section IV D below), one can decide *a priori* how many STO shells are needed in order to describe the wavefunction up to a certain distance from the center of the system.

Given the advantages of the Slater-type orbitals, we attempt to find a set of Gaussian-type orbitals able to reproduce a given number of STO shells. However, in order to avoid the disadvantages of the Kaufmann method, our scheme will not rely on approximating every STO separately. Instead, we will generate a sequence of GTOs such that each STO from a predefined range can be approximated by their linear combination with a roughly equal precision. We also aim at keeping the basis set free from the linear dependencies.

Similarly to the Kaufmann approach, we choose the overlap integral as a criterion of similarity between an STO and a GTO, since it can be associated with the $L^2(\mathbb{R}^3)$ metric in the Hilbert space. By using the orthonormality property of the spherical harmonics, the overlap between two normalized functions of a given l , a GTO with exponent α and a STO with exponent ζ and a principal quantum number n , can be evaluated analytically from the following equation

$$S(n, l, \zeta, \alpha) = \frac{2^{-l/2-1/4} \alpha^{-n/2-l/2-1} \zeta^{n+1/2}}{\sqrt{(2n)!}} \times \\ \times \sqrt{\frac{\alpha^{l+3/2}}{\Gamma(l+3/2)}} \Gamma(n+l+2) U\left(\frac{n+l+2}{2}, \frac{1}{2}, \frac{\zeta^2}{4\alpha}\right), \quad (14)$$

where $U(a, b, z)$ is the confluent hypergeometric function of the second kind [154]. The STO exponent may be viewed as an effective nuclear charge seen by the electron. Since in this paper we focus on the hydrogen atom, from now on we set $\zeta = 1$.

We start our procedure by defining the reference subset $\{\mathbf{S}\}$ of Slater-type orbitals, which we aim at approximating by the Gaussian functions. The choice of this subset depends both on the system under consideration and the simulation conditions. Since the basis set is meant to describe primarily the excited and continuum states, a reasonable choice for the principal quantum number n of the first STO in the subset $\{\mathbf{S}\}$ is the number corresponding to the lowest unoccupied atomic shell. The upper bound of the reference subset is less obvious to define, as it should correspond to the highest energy states achievable by the electron in the applied electric field. One way to estimate it is to take the STO shell with $\langle r \rangle$ equal to or slightly exceeding the electron's quiver amplitude, defined as E_0/ω^2 , where E_0 is the amplitude of the electric field and ω its frequency.

Since the Gaussian exponents are real positive numbers, a brute-force optimization of the whole basis set seems rather impossible. However, we can discretize the range of possible exponents and construct the so-called sampling set, from which we will select functions to be included in the final basis set. This discretization relies on generating a large set of even-tempered Gaussian

(ETG) functions $\{\mathbf{G}\}$ (Gaussian functions with constant ratios between adjacent exponents). The ETG functions possess a useful property of spanning the Hilbert space evenly [155], and are therefore able to approximate any function with accuracy dependent solely on the ratio between exponents. The optimal size and range of the sampling set will be discussed later.

The selection of the exponents from the sampling set $\{\mathbf{G}\}$ is performed separately for each angular momentum. For each l ranging from $l = 0$ to $l = L_{max}$ we calculate a $S \times G$ matrix of overlap integrals between STOs from the reference subset $\{\mathbf{S}\}$ and GTOs from the sampling set $\{\mathbf{G}\}$. First, we need to reject GTOs that have no significant contribution to the description of any STO. We accomplish this by removing the GTOs for which the maximum component of the overlap vector is smaller than the so-called overlap cutoff. Next we calculate the sums of the components of the remaining vectors (their L^1 norms), obtaining for each GTO a quantity that we will refer to as the cumulative performance score,

$$\text{CPS}_i = \sum_{j=1}^S |\langle \chi_j^{\text{STO}} | \chi_i^{\text{GTO}} \rangle|. \quad (15)$$

The cumulative performance score may be seen as a measure of an overall performance of a single GTO in the description of all the STOs. The choice of L^1 norm is based mostly on the intuitiveness of the results. In this way the cumulative performance score can take on values from 0 to S (as we are operating on normalized functions). We can thus deduce from this that the functions with CPS value close to S are most essential for approximating a majority of STOs (i.e. their coefficients in most of the GTO expansions are usually large), while the functions with the cumulative performance score close to zero poorly approximate the STOs or approximate only a few of them. Alternatively, using the L^2 norm or the L^0 norm (measured as the number of components larger than a predefined threshold) may also be considered.

Next we start an iterative procedure of selecting GTOs based on their cumulative performance score:

1. From the remaining GTOs we choose the one with the highest cumulative performance score and include it in the final basis set.
2. Because the initial sampling set should be rather extensive in order to approximate the continuous spectrum of exponents as closely as possible, we usually encounter a large number of GTOs which overlap with the reference subset in a similar manner to the GTO chosen in step 1. In other words, their overlap vectors are close due to similar values of the exponents. The sampling set must be further depleted of these functions before selecting the next GTO, in order to keep the final basis set free of linear dependencies. We achieve this goal by determining the so-called cosine distance between

the overlap vectors of the GTOs. The cosine distance between vectors \mathbf{A} and \mathbf{B} is defined as:

$$D_{\cos}(\mathbf{A}, \mathbf{B}) = 1 - \cos(\mathbf{A}, \mathbf{B}) \quad (16a)$$

$$\cos(\mathbf{A}, \mathbf{B}) = \frac{\mathbf{A} \cdot \mathbf{B}}{\|\mathbf{A}\|_2 \|\mathbf{B}\|_2}. \quad (16b)$$

Its value may range from 0 to 2, however in our case the maximum value is 1, since the overlap integrals are non-negative. When the cosine distance is 1, the overlap vectors are orthogonal, meaning that the function described by the vector \mathbf{A} overlaps with different STOs than function described by the vector \mathbf{B} . When the cosine distance equals 0, the overlap vectors are parallel (differing only by a proportionality constant), meaning that both functions approximate the same STOs. Therefore, one of the functions is redundant and may be eliminated. In our procedure we first calculate the cosine distances between the overlap vector corresponding to the function chosen in step 1 and the overlap vectors of all the remaining GTOs.

3. Next we introduce the so-called cosine cutoff, a value of which determines the maximum acceptable similarity between two overlap vectors (and thereby also between two basis functions). The GTOs for which the cosine distance calculated in step 2 is smaller than the cosine cutoff are removed.

Steps 1-3 are repeated until all of the GTOs are either removed or included to the final basis set.

Since the core element of our method is defining the range of states that are energetically accessible by the electron, for a basis set constructed according to the above scheme we propose the name of active range-optimized (ARO) basis set.

The most critical factor in constructing an optimal ARO basis set is the proper choice of the sampling set, i.e., the range of the exponents and the sampling density (the ratio between adjacent exponents). If this range is too narrow or ill-placed, some of the STOs, especially with the lowest or highest n , may not be described properly due to the lack of sufficiently diffuse or tight functions. Choosing a range which is too broad should not affect the final outcome, since any redundant functions will be removed anyway due to the overlap cutoff condition, but it may significantly extend the computational time. Since in our scheme each STO is approximated by a linear combination of GTOs, some functions with relatively large and small exponents may actually be beneficial for a more accurate description. Therefore, a reasonable guess for the sampling set range should be the range covering the exponents of the Kaufmann functions fitting the same reference subset (for the hydrogen atom, approximately from 10^{-4} to 10^0), but extended on both sides by one or two orders of magnitude. The appropriateness of this choice can easily be verified by checking if at least

a few of the functions are discarded due to the overlap cutoff condition. As we mentioned in the step 2 of the iterative procedure, the sampling density should be high enough to provide convergence with respect to the number of functions in the final ARO basis set and the values of the selected exponents. In our calculations about 10 000 ETG functions with exponents ranging between 10^{-k} and 10^{-k+1} usually proved sufficient to achieve this convergence.

The overlap cutoff governs the number of “enhancing” functions mentioned above, i.e. the tight and diffuse GTOs that usually do not have any major contribution to the description of STOs, but merely improve the GTO approximation. The proper choice of the overlap cutoff provides the optimal effective range of exponents from which the functions are selected. Our calculations have shown that values between 0.1 and 0.2 is appropriate.

The cosine cutoff determines the overall number of functions in the final basis set. As previously stated, it also serves as a tool for reducing the linear dependencies in the basis set. It is important to emphasize that these features are achieved not by limiting the similarity of the Gaussian functions themselves, but by limiting the similarity with which two GTOs describe the reference subset. This unique property is the source of the characteristic structure of the ARO basis sets. Any variation in the exponent of a Gaussian function leads to changes in the overlap integrals and therefore to a change in the orientation in the overlap vector by a certain angle. In our procedure the cosine of this angle is compared to the cosine cutoff in order to decide whether a certain function from the sampling set is to be removed or kept for further selection. However, it is interesting to note that the value of this angle depends not only on the variation in the exponent, but also on the values of the overlap vector components. Functions that have a large contribution to the majority of the reference subset usually correspond to overlap vectors with most of the components significantly larger than zero. Therefore, a change of an exponent, even a relatively small one, results in varying the majority of the overlap vector components. The combination of small variations in a large number of components may already suffice to fulfill the cosine cutoff condition. On the contrary, the “enhancing” functions usually correspond to overlap vectors with most of the components close to zero, thus a small variation in the exponent changes only a few components of the overlap vector. It is therefore clear that a much larger variation needs to be applied in order to alter the orientation of the overlap vector by an angle sufficient to fulfill the cosine cutoff condition. A direct consequence of this fact is that in the ARO basis sets the ratios between adjacent exponents are the largest for the most tight and diffuse functions. This ensures the densest distribution of functions that play a key role in approximating the reference subset, as compared to the “enhancing” functions. This feature distinguishes the ARO basis set from the Kaufmann basis set, where the ratios between adja-

cent exponents decrease with their values, as well as from the ETG basis sets, where this ratio is constant for all adjacent functions.

IV. COMPUTATIONAL DETAILS

A. Simulation conditions

We performed a series of real-time propagations of the hydrogen atom wavefunction in short (femtosecond-scale) intense pulses of a linearly polarized laser field, represented by an oscillating electric field. The nucleus is considered at rest. The interaction between the electron and the external field is treated in the dipole approximation. The calculations are performed in the velocity gauge, as it requires lower angular momenta included in the basis set for the results to converge than in the length gauge [156]. The interaction operator $V_{\text{ext}}(t)$, coupling the electron and the electric field polarized along the z -axis, reads $V_{\text{ext}}(t) = -iA(t)\frac{\partial}{\partial z}$ in the velocity gauge, where $A(t)$ is the vector potential related to the field $E(t)$ by the relation $E(t) = -\partial_t A(t)$. In our calculations the vector potential corresponds to a time-dependent electric field representing a laser pulse with a sine-squared envelope:

$$E(t) = \begin{cases} E_0 \sin(\omega_0 t) \sin^2(\omega_0 t/2n_c) & \text{if } 0 \leq t \leq 2\pi n_c/\omega_0, \\ 0 & \text{otherwise,} \end{cases} \quad (17)$$

where E_0 is the field amplitude related to the laser peak intensity I_0 by $I_0 = \epsilon_0 c E_0^2$, ω_0 is the carrier frequency, and n_c is the number of optical cycles the pulse consists of. As it can be deduced from the above equation, $2\pi n_c/\omega_0$ is the total duration of the pulse.

All calculations are performed for $\omega_0 = 1.55$ eV ($\lambda = 800$ nm), corresponding to a Ti:sapphire laser, frequently used in the attosecond experiments [1]. The number of optical cycles is either 4 or 20 (corresponding to time intervals of approximately 441.3 and 2206.6 a.u.). The barrier-suppression ionization threshold of the hydrogen atom (the intensity sufficient for the electron to classically overstep the potential barrier generated by the nucleus) is about 1.37×10^{14} W/cm². We examine four laser intensities, two below the ionization threshold, 5×10^{13} W/cm² and 1×10^{14} W/cm², and two above it, 2×10^{14} W/cm² and 5×10^{14} W/cm².

In order to capture the ionization process, a complex absorbing potential (CAP) of the form $-iV_{\text{CAP}}(r)$ is also included in the time-dependent Hamiltonian. The structure of the applied CAP is discussed below.

To sum up, the total expression for the time-dependent Hamiltonian, in atomic units, reads

$$H(\mathbf{r}, t) = -\frac{1}{2}\nabla^2 - \frac{1}{r} - iA(t)\frac{\partial}{\partial z} - iV_{\text{CAP}}(r), \quad (18)$$

where r denotes the distance between the electron and the nucleus.

B. Basis set calculations

The basis set calculations are performed using three different ARO basis sets, constructed according to the scheme presented in Section III and fitted to reference subsets of STOs with principal quantum numbers ranging from 2 to either 30, 60, or 90. Each basis set includes functions with angular momenta from 0 (s -type orbitals) to 8 (l -type orbitals). The sampling set is the same for each basis set and each angular momentum, and comprises of 10000 ETG functions, with exponents ranging from 10^{-6} to 10^1 . The overlap cutoff was empirically set to 0.15, a value that provided the best results. The cosine cutoff was adjusted separately for each angular momentum in each basis set, so that in every basis set the number of functions with a given l is equal to 19 for $l = 0$ or $l - 1$ for $l \geq 1$. In this way the correct degeneracy of the unoccupied orbitals of the hydrogen atom is reproduced. In order to properly describe the ground state of the hydrogen atom, each basis set was supplemented with the 1s orbital from the STO-6G hydrogen basis set, which is a contraction (a linear combination with fixed coefficients) of six Gaussian functions.

For comparison, we constructed a Kaufmann basis set, also containing functions with nine lowest angular momenta, fitted to STOs with principal quantum numbers from 2 to 20. The STO-6G hydrogen orbital was also added to this basis set. It can be seen that the number of functions is equal for both kinds of basis sets, which ensures a fair comparison of the results. We extended the results of Kaufmann (who provides the Gaussian exponents up to $l = 5$ only [137]), by finding numerical roots of the derivatives of $S(n, l, \zeta, \alpha)$, Eq. (14), with respect to α for different values of n and l , with the Anderson-Björk algorithm implemented in the mpmath Python library [157].

The ground state of the system is obtained through the diagonalization of the Hamiltonian matrix in each of the constructed basis sets, in the absence of the external electric field and the complex absorbing potential. The real-time propagation is performed afterwards, starting from the generated ground state. In the case of the hydrogen atom, due to the cylindrical symmetry of the Hamiltonian in (18), only orbitals with the projection of the orbital angular momentum parallel to the linearly polarized electric field are coupled to it and contribute to the dipole moment. Therefore, in order to speed up the calculations, we use only functions with $m = 0$.

Formally, the propagation scheme presented in Eq. (4) involves a time-ordered matrix exponential which is extremely challenging to calculate. To avoid this, the propagator is calculated in timesteps of Δt , using the Crank-

Nicolson propagator [158]:

$$U(t + \Delta t, t) = \left(1 + \frac{i\Delta t}{2}H(t + \Delta t/2)\right)^{-1} \times \left(1 - \frac{i\Delta t}{2}H(t + \Delta t/2)\right), \quad (19)$$

so the matrix propagation equation changes to

$$\left(\mathbf{I} + \frac{i\Delta t}{2}\mathbf{H}(t + \Delta t/2)\right)\mathbf{c}(t + \Delta t) = \left(\mathbf{I} - \frac{i\Delta t}{2}\mathbf{H}(t + \Delta t/2)\right)\mathbf{c}(t), \quad (20)$$

where \mathbf{I} is the identity matrix. The timestep is set to 0.01 a.u. and the total propagation time is equal to twice the duration of the pulse.

C. Grid-based calculations

As a numerical reference, we also performed grid-based real-time propagation of the hydrogen atom using the QPROP software [159, 160]. These calculations are also performed in the velocity gauge. In QPROP the hydrogen atom wavefunction is expanded in partial waves (spherical harmonics multiplied by the corresponding radial functions):

$$\Psi(\mathbf{r}, t) = \frac{1}{r} \sum_{l=0}^{L_{max}} \sum_{m=-l}^{m=l} R_{lm}(r, t) Y_{lm}(\theta, \phi) \quad (21)$$

In our calculations we expand the wavefunction in $L_{max} = 40$ partial waves, which are sufficient to achieve the convergence of the results (the HHG spectra and the ionization probabilities) for all investigated laser intensities. The radial grid extends to 120 bohr, with the spacing set to 0.1 bohr. The timestep and the total propagation time are the same as in the basis set calculations.

D. The complex absorbing potential

Because the Gaussian basis sets are not complete, due to a finite number of both angular and radial functions, they are not able to properly describe the wavefunction at an arbitrary distance from the nucleus. This causes unphysical reflections of parts of the wavefunction associated with the continuum eigenstates and their interference with the bound states. A similar problem is encountered in the grid-based approach, where the wavefunction is reflected after reaching the grid boundary. The most common way to avoid such artifacts is to use a complex absorbing potential, which effectively eliminates the components of the wavefunction that travel further away from the center of the system than a predefined distance r_{CAP} , simulating the ionization process [161, 162]. Since

the introduction of the CAP breaks the conservation of the norm of the wavefunction, the time propagation is no longer unitary. In many applications the CAP introduced by Manolopoulos [163], which has a sound mathematical basis, is used [164–167]. Unfortunately, this potential cannot be applied in any basis set calculations, since it contains a singularity which causes the matrix elements of V_{CAP} to diverge. This difficulty can be overcome by using a polynomial form for the CAP. Thus, in both the basis set calculations and the grid-based calculations we implement a quadratic CAP of the form

$$V_{CAP}(r) = \eta \theta(r - r_{CAP}) (r - r_{CAP})^2, \quad (22)$$

where $\theta(r)$ is the Heaviside step function and r_{CAP} denotes the starting position of the CAP. The parameter $\eta = 2.4 \times 10^{-4}$ was optimized to reproduce the results obtained on a grid with the CAP derived by Manolopoulos [163]. The details of the construction of the CAP and its properties are presented in the Appendix.

The choice of the CAP starting position is not unique and it can strongly affect the final results, especially the ionization probability. In some studies, r_{CAP} is defined by the quiver amplitude of the electron in the oscillating electric field, and thus depends on the simulation conditions [77, 168, 169]. In others, it is placed more arbitrarily, e.g. based on the van der Waals radius of the examined atom [170]. In the present paper we propose a universal method for determining an optimal r_{CAP} , which depends only on the simulated system and not on the external perturbation. It can simultaneously be derived based on three different premises:

1. The first reasoning is purely theoretical. For any atom we can define a critical electric field strength above which the electron can escape the Coulomb potential of the nucleus in a classical manner, and the ionization mechanism switches from the tunneling ionization to the barrier-suppression ionization [171]. For hydrogen-like ions the value of this field is usually defined as $E_{crit} = Z^3/16$, so for the hydrogen atom we obtain $E_{crit} = 0.0625$ a.u., which corresponds to the previously mentioned value of intensity 1.37×10^{14} W/cm². Since the three-step model of HHG involves the tunneling step, we can assume that only the electron trajectories that do not exceed the quiver amplitude associated with E_{crit} contribute to the harmonic generation. We can thus define r_{CAP} as the critical field quiver amplitude, which for the hydrogen atom is equal to 19.3 bohr.
2. The CAP starting position should be located in a range where the asymptotic ionization probability measured at the end of the time propagation is invariant with respect to r_{CAP} . We performed a series of grid-based propagations for the hydrogen atom using our CAP with r_{CAP} varying from 5 to 35 bohr, and found this range to be about 9 to

21 bohr. A similar reasoning concerning the invariance of the ionization rates with respect to r_{CAP} was adopted by Sissay et al., who achieved results consistent with ours [172].

3. The optimal value of r_{CAP} should also maximize the relative height difference between the harmonic plateau and the background beyond the harmonic cutoff, leading to the sharpest cutoff. Placing the CAP starting position too close from the nucleus eliminates some of the electron trajectories that should end in the recombination and harmonic generation, lowering the intensities of harmonic peaks. Similarly, placing it too far from the nucleus spuriously includes some trajectories of the ionized electron in the HHG process, elevating the background. By performing similar test calculations as in the previous point, we determined the value of r_{CAP} that maximizes the cutoff height to be about 19 bohr.

It can be seen that all three approaches lead to a similar value of the optimal r_{CAP} , which is about 19 bohr. In our calculations we extend this value to 19.5 bohr in order to ensure that the CAP minimally overlaps with the bound eigenstates.

V. RESULTS

A. Time-independent calculations

Before comparing the results obtained via the real-time propagation, we first focus on the general properties of the ARO basis sets, in particular their ability to approximate the time-independent Hamiltonian eigenspectrum of the hydrogen atom. This provides us a preliminary assessment of their potential to describe the evolution of the time-dependent wavefunction. The characteristics of each of the constructed ARO basis sets (named ARO30, ARO60 and ARO90, based of the maximum principal quantum number of the Slater orbital in the respective reference subset), compared with the Kaufmann basis set (analogously named K20), are presented in Tab. I. As predicted, the ARO construction scheme encompasses a much wider range of GTO exponents. This range also shifts towards smaller exponents as the reference subset is extended since the STOs with higher principal numbers are characterized by larger values of $\langle r \rangle$. Due to this fact, the ARO basis sets are practically free of linear dependencies. Of the three examined basis sets only ARO30 required a removal of 5 linear combinations of GTOs in order to avoid numerical instabilities during the diagonalization of the Hamiltonian matrix, while in the case of the K20 basis set this number exceeds 40.

Interestingly, extending the reference subset of the ARO basis sets increases the number of bound Hamiltonian eigenstates, at the expense of the number of continuum eigenstates. However, at the same time the highest

Hamiltonian eigenvalue also tends to rapidly decrease, resulting in a denser distribution of the states just above the ionization potential (which should be crucial in simulations with fields close to the ionization threshold). The highest number of continuum eigenstates per unit of energy is still achieved using the K20 basis set, but the number of bound states generated by this basis set is far smaller compared to each of the ARO basis sets.

The energies of the first few hydrogen orbital energies are presented in Tab. II. In general, each of the ARO basis sets provides more accurate energies of the hydrogen orbitals than the K20 basis set. The degeneracies of the atomic shells are also reproduced more faithfully. The number of correctly described shells increases with the ARO reference subset size and for the ARO90 basis set we obtain an excellent agreement with the exact energies up to $n = 10$. It is also worth noticing that apart from increasing accuracy of the high energy states, the accuracy of the lowest eigenvalues tends to decrease slightly. Although seemingly worrying, this may actually indicate that the ultimate purpose and motivation behind the ARO construction scheme - the ability of the basis set to reproduce as many eigenstates as possible with a comparable accuracy - strives to be fulfilled.

B. Real-time propagations

In this subsection we discuss the quality of the results obtained via the real-time propagation of the hydrogen atom wavefunction using the constructed ARO basis sets. Let us start by analysing the effect of the size of the ARO reference subset on real-time observables. The exemplary HHG spectra and ionization probabilities calculated using the ARO30, ARO60 and ARO90 basis sets for the case of $I_0 = 2 \times 10^{14} \text{ W/cm}^2$ and $n_c = 4$ are presented on Fig. 1. It can easily be seen that extending the ARO reference subset crucially improves the quality of the HHG spectrum, reducing the noises in the HHG background beyond the harmonic cutoff. It also has a positive effect on the presence and position of the cutoff itself. In the spectrum obtained using the ARO30 basis set the cutoff is barely distinguishable, as the intensities of the subsequent harmonic peaks decrease incrementally with increasing the harmonic order. In the spectrum corresponding to the ARO60 basis set the cutoff is already visible, but located too far compared to the numerical result (between 50th and 60th harmonic). Finally, in the ARO90 spectrum the cutoff is not only clearly visible, but also matches both the grid-based results and the theoretical value of 33rd harmonic.

The effect of the size of the reference subset on the ionization probability is less striking. It can be seen that along with adding more STOs the curves become more ridged and the inflection points corresponding to the consecutive optical cycles become more distinct, resembling the grid-based results.

Since of all the examined ARO basis sets the ARO90

TABLE I. The characteristics of the ARO basis sets and the Kaufmann basis set used throughout the calculations.

	ARO30	ARO60	AR090	K20
Number of basis set functions ¹	144	144	144	144
Number of linearly independent functions ^{1,2}	139	144	144	101
Lowest exponent ³	6.048084×10^{-4}	7.329910×10^{-5}	9.702192×10^{-6}	1.711786×10^{-3}
Highest exponent ³	1.969985	1.229846	8.045241×10^{-1}	1.012151×10^{-1}
Number of bound Hamiltonian eigenstates ($E < 0$)	31	47	64	23
Number of continuum Hamiltonian eigenstates ($E > 0$)	108	97	80	78
Lowest Hamiltonian eigenvalue (ground state energy)	-0.499908	-0.499907	-0.499905	-0.498694
Highest Hamiltonian eigenvalue	21.88196	12.60912	7.71554	0.98572

¹ only functions with $m = 0$ counted² with the threshold for the minimal overlap matrix eigenvalue equal to 10^{-8} ³ not counting the STO-6G 1s orbital

TABLE II. Few lowest orbital energies calculated with the used basis sets. The dashes denote that none of the computed Hamiltonian eigenvalues can be attributed to a given hydrogenic state

Orbital	Exact value	ARO30	ARO60	AR090	K20
1s	-0.5	-0.499908	-0.499907	-0.499905	-0.498694
2s	-0.125	-0.124995	-0.124993	-0.124987	-0.124450
2p	-0.125	-0.124988	-0.124988	-0.124986	-0.124314
3s	-0.0(5)	-0.055556	-0.055556	-0.055556	-0.055551
3p	-0.0(5)	-0.055554	-0.055553	-0.055552	-0.055359
3d	-0.0(5)	-0.055552	-0.055552	-0.055551	-0.055304
4s	-0.03125	-0.031250	-0.031250	-0.031250	-0.031243
4p	-0.03125	-0.031250	-0.031250	-0.031250	-0.031240
4d	-0.03125	-0.031249	-0.031249	-0.031248	-0.031163
4f	-0.03125	-0.031249	-0.031249	-0.031248	-0.031137
5s	-0.02	-0.019999	-0.020000	-0.020000	-0.019904
6s	-0.013(8)	-0.013881	-0.013889	-0.013889	-0.012559
7s	-0.010204	-0.009933	-0.010204	-0.010204	-
8s	-0.007813	-	-0.007812	-0.007812	-
9s	-0.006173	-	-0.006070	-0.006173	-
10s	-0.005	-	-	-0.004992	-

one provides clearly the best results, for the sake of clarity and transparency in the further discussion we no longer analyse the results obtained using the ARO30 and ARO60 basis sets.

A comparison of the HHG spectra obtained using the ARO90 basis set, the K20 basis set, and the grid-based calculations for all simulation conditions considered here is presented in Fig. 2. It can be seen that in all cases except $I_0 = 5 \times 10^{14}$ W/cm² and $n_c = 20$ the ARO90 basis set predicts the cutoff position closer to the theoretical reference than the K20 basis set. The K20 basis set performs particularly underwhelmingly at the intensities below the ionization threshold, as the harmonic peaks are present even after twice the theoretical cutoff position. The ARO90 is also observed to reproduce the shapes of the lowest harmonic peaks more accurately.

Not to rely solely on the visual assessment of the spectra, we should introduce a quantitative measure that will allow us to quantify how accurately each of the basis sets

reproduces the spectrum obtained using the grid-based calculations. No such measure for comparing the HHG spectra has been proposed in the literature thus far. Our suggestion is to treat the HHG spectrum as any other signal and apply tools known from the signal processing. A common method for determining the similarity of two signals relies on the so-called correlation distance, which for signals \mathbf{A} and \mathbf{B} is defined as

$$D_{\text{corr}}(\mathbf{A}, \mathbf{B}) = 1 - \frac{(\mathbf{A} - \bar{\mathbf{A}}) \cdot (\mathbf{B} - \bar{\mathbf{B}})}{\|(\mathbf{A} - \bar{\mathbf{A}})\|_2 \|(\mathbf{B} - \bar{\mathbf{B}})\|_2}, \quad (23)$$

where $\bar{\mathbf{A}}$ and $\bar{\mathbf{B}}$ are the mean values of the signals \mathbf{A} and \mathbf{B} . One can immediately notice the resemblance to the previously introduced cosine distance (16). The only difference is that the correlation distance includes the mean values of the signals and thus it is insensitive to shifting the signals along the y axis. In comparing the HHG spectra this is more appropriate, since we are interested only in the relative differences between values at given points on the x axis (e.g. the presence of the harmonic peaks beyond the theoretical cutoff position). Similarly to the cosine distance, the correlation distance can also assume values from 0 to 2. For $0 < D_{\text{corr}} < 1$ the signals are positively correlated, for $D_{\text{corr}} = 0$ there is no (either positive or negative) correlation between the signals, and for $1 < D_{\text{corr}} < 2$ the signals are negatively correlated. Because the intensity of the lowest harmonics is usually larger by several orders of magnitude than the intensity of the highest ones, we use the decimal logarithms of the spectra, so that the correlation distance depends on the whole shape of the spectrum and not only on the shapes of the few highest peaks. The correlation distances between the spectra obtained from the basis set calculations and from the grid-based calculations are presented in Tab. III. It can be seen that for all simulation conditions the ARO90 basis set provides a better agreement with the numerical reference than the K20 basis set, with the correlation distance being over two times smaller.

In terms of the ionization probability of the hydrogen atom, the ARO90 basis set also provides a good quantitative agreement with the numerical reference, as presented in Fig. 3. The largest discrepancy is observed for

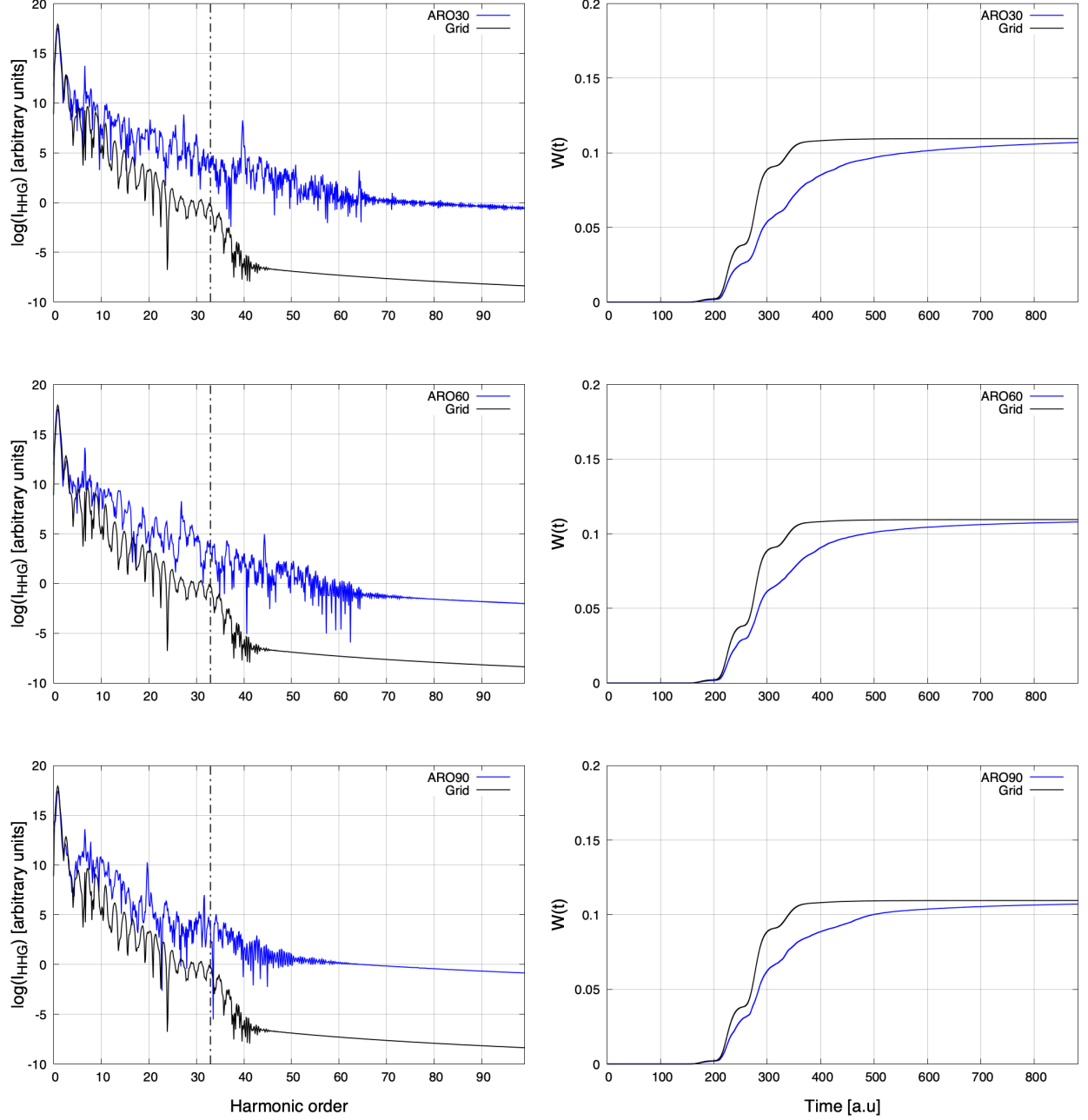


FIG. 1. HHG spectra (left column) and ionization probabilities (right column) of the hydrogen atom at $I_0 = 2 \times 10^{14}$ W/cm² and $n_c = 4$, obtained using three different ARO basis sets, compared with the grid-based results. The HHG spectra are presented up to thrice the harmonic cutoff value (denoted by the dot-dashed line)

$I_0 = 5 \times 10^{14}$ W/cm² and $n_c = 4$, where the ionization probability at the end of the simulation differs from the grid-based result by about 10%. However, the overall shape of the curve is still reproduced well. The ARO90 basis set performs better than the K20 basis set, especially for the lower two intensities, for which the latter tends to hugely overestimate the ionization probability. This may be attributed to the poor description of the

bound excited states by the K20 basis set. The lack of functions with sufficiently large GTO exponents causes the wavefunction to dissipate unphysically and become absorbed by the CAP at a higher rate. For the intensities above the ionization threshold the results obtained using the two basis sets are comparable, although some details in favor of the ARO20 basis set can be pointed out. The latter provides a better behavior of the ioniza-

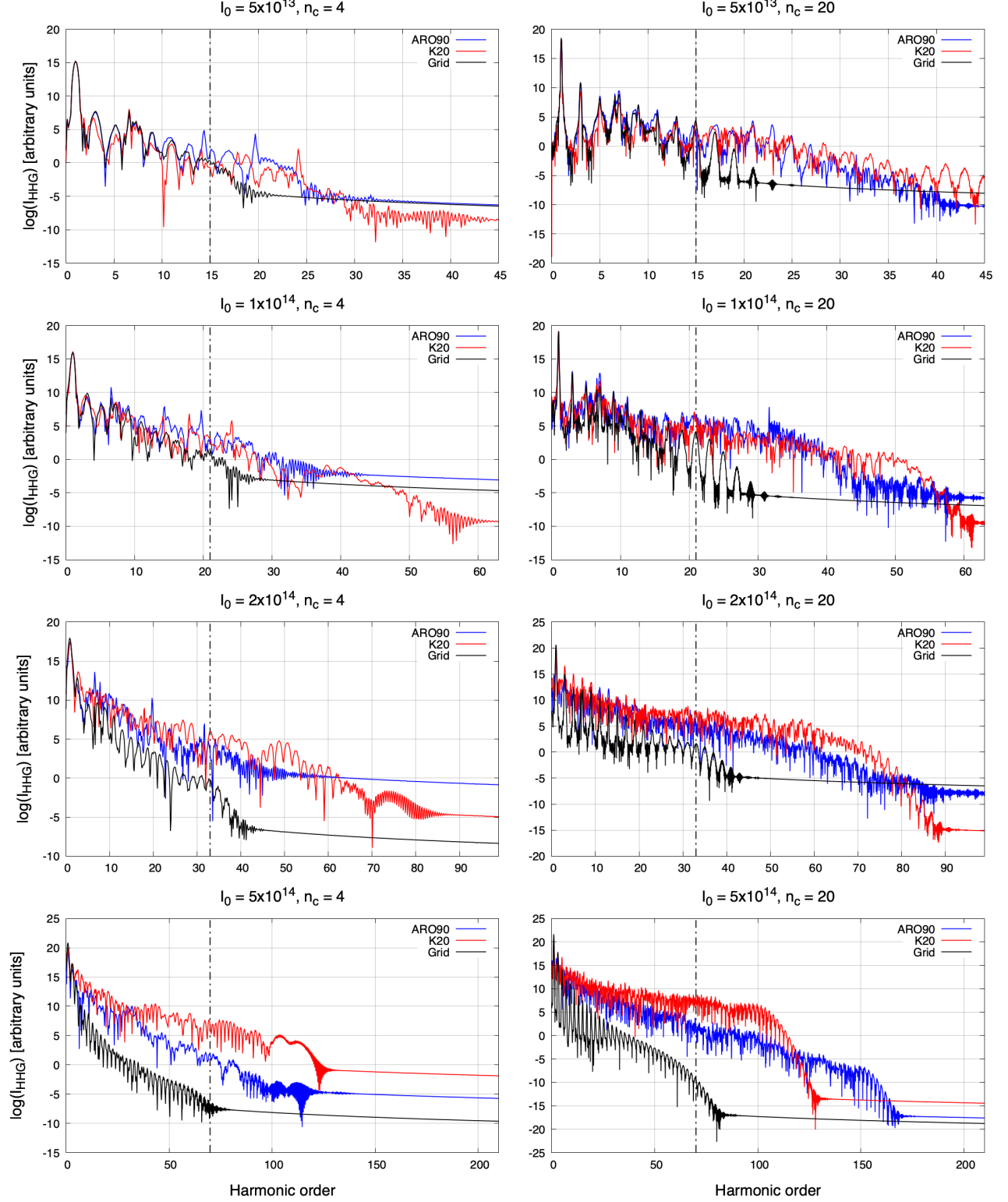


FIG. 2. HHG spectra of the hydrogen atom at different laser intensities and different numbers of optical cycles, obtained using the ARO90 basis set, using the K20 basis set, and from the grid-based calculations. The spectra are presented up to thrice the harmonic cutoff value (denoted by the dot-dashed line)

TABLE III. The correlation distances between the HHG spectra obtained from the basis set calculations and from the grid-based calculations, for different simulation conditions. When calculating the correlation distance the spectra were truncated at the harmonic order equal to thrice the harmonic cutoff.

I_0	n_c	ARO90	K20
5×10^{13}	4	0.06775	0.09879
	20	0.16025	0.22143
1×10^{14}	4	0.06179	0.13208
	20	0.19953	0.21976
2×10^{14}	4	0.04491	0.11820
	20	0.15215	0.31249
5×10^{14}	4	0.07507	0.13754
	20	0.16756	0.22046

tion probability at the beginning of the simulation, where in case of the K20 basis set the norm of the wavefunction begins to decrease too early. Additionally, the constant behavior of the ionization probability at the end of the simulations, observed both in the ARO90 basis set calculations and the grid-based calculations, is not obtained using the K20 basis set.

VI. CONCLUSION

In this paper, we introduced a novel systematic scheme for the construction of the Gaussian basis sets that are suitable to describe atomic and molecular excited and continuum states. Similarly to the approach presented by Kaufmann *et al.* [137], our approach has strong theoretical foundations, but it also bypasses most of the limitations related to the use of the K functions. Using the ARO basis sets we are able to quantitatively or semi-quantitatively reproduce the HHG spectra of the hydrogen atom for intensities below and slightly above the ionization threshold, especially for the shorter exciting pulses. For the intensity well above the ionization threshold and for longer laser pulses there are some discrepancies observed, especially in the harmonic cutoff position. However, in most cases they are notably smaller than using the Kaufmann basis set. The ARO basis sets also enable a very good description of the ionization probability at practically all intensities.

The results obtained with the ARO basis sets constructed using different reference subsets explicitly show that a large range of Slater orbitals is required to properly approximate the time-dependent wavefunction, even if the laser intensity is relatively low. The omission of STOs with high principal numbers, which is inevitable in the approach proposed by Kauffman *et al.*, leads to a notable worsening of the HHG spectra.

The promising results obtained here for the hydrogen atom indicate that the ARO basis set can also be applied to more complex systems. It should be noted that

for many-electron atoms the ARO construction scheme remains essentially the same: the sole difference is the STO exponent ζ , which should be replaced by an effective nuclear charge of the atom under consideration. In a future work we plan to present results of the calculations for several many-electron systems, including multicenter molecules, starting with the simplest ones, namely the helium atom and the dihydrogen molecule.

It should be emphasised that in the present paper we focus on basis sets containing only one type of functions describing the excited and continuum states (either ARO functions or the K functions). We do not rule out the possibility that even better results can be obtained by combining the ARO basis set with some other Gaussian basis sets, analogously to the extensions of the K functions by Luppi *et al.* [145–150]. This subject will also be explored in future works.

This paper also presents a self-consistent method to determine the optimal CAP starting position by utilizing three different approaches: the semiclassical quiver amplitude of the electron in the electromagnetic field, the convergence of the ionization probability and the optimization of the shape of the HHG spectrum. We also introduce a quantitative measure for comparing the HHG spectra based on the correlation distance, which, to our knowledge, is the first to appear in the literature.

ACKNOWLEDGMENTS

We acknowledge the Polish National Science Center (Grant No. 2016/20/W/ST4/00314), Spanish Ministry MINECO (National Plan 15 Grant: FISICATEAMO No. FIS2016-79508-P, SEVERO OCHOA No. SEV-2015-0522, FPI), European Social Fund, Fundació Cellex, Fundació Mir-Puig, Generalitat de Catalunya (AGAUR Grant No. 2017 SGR 1341, CERCA/Program), ERC AdG NOQIA, EU FEDER, European Union Regional Development Fund - ERDF Operational Program of Catalonia 2014-2020 (Operation Code: IU16-011424) and MINECO-EU QUANTERA MAQS (funded by The State Research Agency (AEI) PCI2019-111828-2 / 10.13039/501100011033).

Appendix: Construction of the complex absorbing potential

In this appendix we describe a derivation of the complex absorbing potential used in our calculations. The CAP developed by Manolopoulos [163] has a complicated form expressed through the Jacobi elliptic functions, but for practical purposes it can be approximated as

$$V_{\text{CAP}}^M(r) = E_{\min} \theta(r - r_{\text{CAP}})y(x), \quad (\text{A.1a})$$

$$y(x) = ax - bx^3 + \frac{4}{(c-x)^2} - \frac{4}{(c+x)^2}, \quad (\text{A.1b})$$

$$x = 2\delta k_{\min}(r - r_{\text{CAP}}). \quad (\text{A.1c})$$

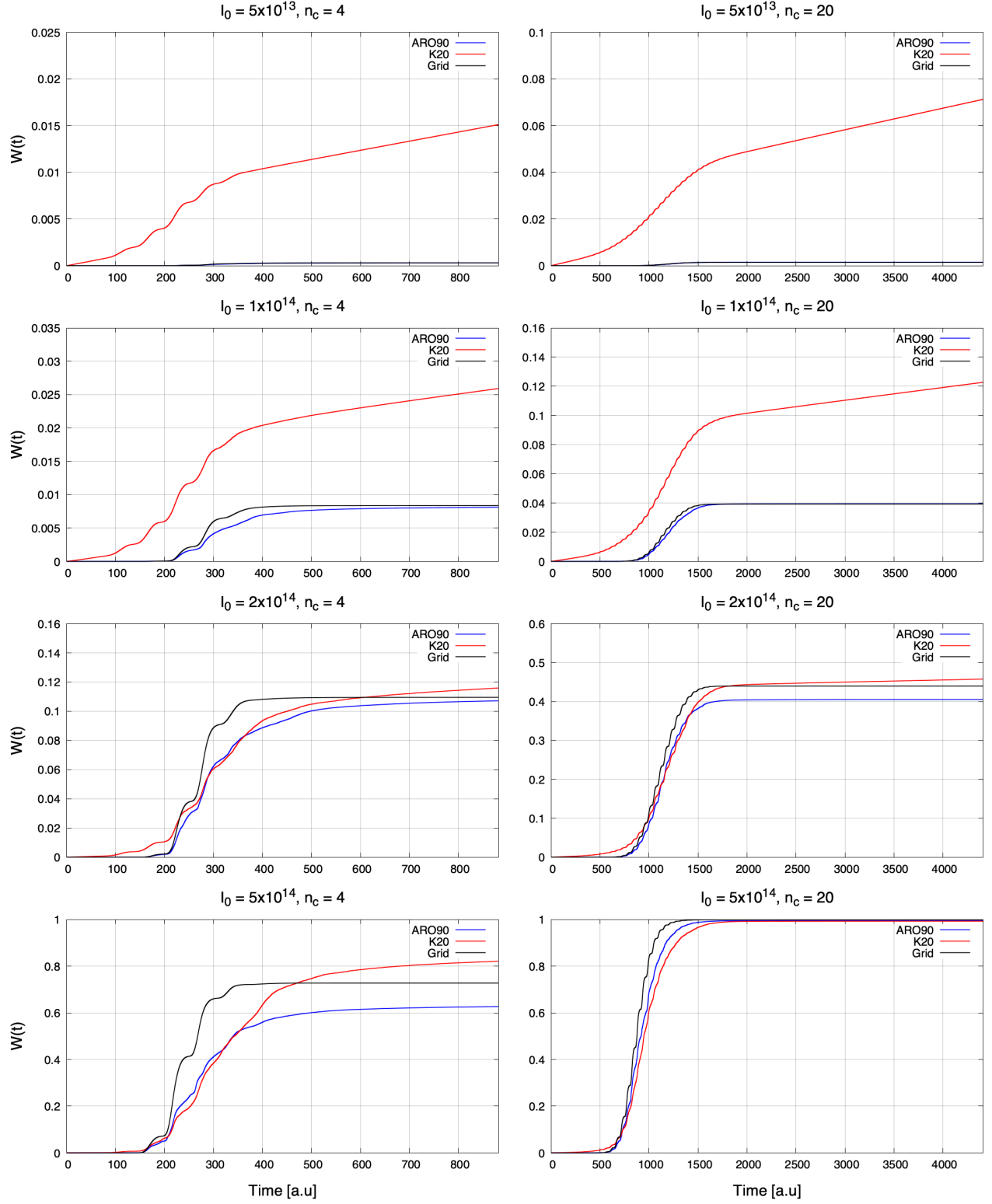


FIG. 3. Ionization probabilities of the hydrogen atom at different laser intensities and different numbers of optical cycles, obtained using the ARO90 basis set, using the K20 basis set, and from the grid-based calculations.

The constants a , b and c are defined in Ref. [163]. This potential was specifically designed to minimize the transmission and reflection and maximize the absorption of the wavefunction. The absorption efficiency is governed by two parameters, δ and k_{\min} , which are connected to the minimum energy E_{\min} the wavefunction needs to possess in order to be absorbed. Unfortunately, due to a singularity at $x = c$, this potential is applicable only in grid-based approaches, where the singular point is usually placed at the grid boundary.

A frequently used alternative is the so-called monomial CAP

$$V_{\text{CAP}}(r) = \eta \theta(r - r_{\text{CAP}}) (r - r_{\text{CAP}})^o \quad (\text{A.2})$$

of order o , which is free of singularities, but at the cost of lower flexibility and a less intuitive construction. However, from the perspective of the basis set calculations, another important advantage of the monomial CAP is that the necessary CAP integrals $\langle \chi_{lm;\alpha}^{\text{GTO}} | V_{\text{CAP}} | \chi_{l'm';\alpha'}^{\text{GTO}} \rangle$ can be evaluated analytically. After inserting the general GTO expression (1) into the matrix element and applying the binomial expansion one obtains a sum of integrals of the form

$$\begin{aligned} f &= N \int_0^\infty \theta(r - r_{\text{CAP}}) r^{2l+o-t+2} \exp(-(\alpha + \alpha')r^2) dr \\ &= N \int_{r_{\text{CAP}}}^\infty r^{2l+o-t+2} \exp(-(\alpha + \alpha')r^2) dr. \end{aligned} \quad (\text{A.3a})$$

$$N = \eta N_\alpha N_{\alpha'} \binom{o}{t} (-r_{\text{CAP}})^t \quad (\text{A.3b})$$

where N_α and $N_{\alpha'}$ are the GTO normalization constants and t can take on values from 0 to o . These integrals have a general solution

$$f = N \frac{r_{\text{CAP}}^{2l+o-t+3}}{2} E_{\frac{1-n}{2}}(r_{\text{CAP}}^2(\alpha + \alpha')), \quad (\text{A.4})$$

where $E_n(z)$ is the generalized exponential integral function [154].

Because the integrals (A.4) have to be evaluated using an extremely high precision we use the monomial CAP with $o = 2$ to reduce the computational costs. The parameter η was determined by performing a series of grid-based calculations and choosing the value which best reproduces the observables: the norm of the wavefunction and the HHG spectra, obtained with the Manolopoulos CAP with $\delta = 0.2$ and $k_{\min} = 0.2$. The optimal value was found to be 2.4×10^{-4} and proved insensitive to the laser intensity.

It is worth mentioning that although the obtained potential behaves very similarly to the Manolopoulos CAP for small $(r - r_{\text{CAP}})$, it rises far more slowly for large $(r - r_{\text{CAP}})$, which may lower the overall absorption efficiency in the grid-based calculations. In order to compensate for it, the width of the absorbing layer (the distance between the CAP starting position and the grid boundary) must be suitably increased. In our calculations an increase from 32.8 bohr in case of the Manolopoulos CAP (a value determined by its parameters) to 100 bohr in case of the monomial CAP proved sufficient to reduce any artifacts resulting from partial reflections of the wavefunction. This problem, however, is absent in the basis set calculations, where the integration of the matrix elements is performed over the whole radial axis.

-
- [1] P. Agostini and L. F. Dimauro, Rep. Prog. Phys. **67**, 813 (2004).
 - [2] P. B. Corkum and F. Krausz, Nat. Phys. **3**, 381 (2007).
 - [3] F. Krausz and M. Ivanov, Rev. Mod. Phys. **81**, 163 (2009).
 - [4] A. McPherson, G. Gibson, H. Jara, U. Johann, T. S. Luk, I. A. McIntyre, K. Boyer, and C. K. Rhodes, J. Opt. Soc. Am. B **4**, 595 (1987).
 - [5] M. Ferray, A. L'Huillier, X. F. Li, L. A. Lompre, G. Mainfray, and C. Manus, J. Phys. B **21**, L31 (1988).
 - [6] J. L. Krause, K. J. Schafer, and K. C. Kulander, Phys. Rev. Lett. **68**, 3535 (1992).
 - [7] P. B. Corkum, Phys. Rev. Lett. **71**, 1994 (1993).
 - [8] K. C. Kulander, K. J. Schafer, and J. L. Krause, in *Super-Intense Laser Atom Physics*, NATO Advanced Studies Institute Series B: Physics, Vol. 316, edited by B. Piraux, A. L'Huillier, and K. Rzażewski (Plenum, New York, 1993) pp. 95–110.
 - [9] M. Lewenstein, P. Balcou, M. Y. Ivanov, A. L'Huillier, and P. B. Corkum, Phys. Rev. A **49**, 2117 (1994).
 - [10] E. Constant, D. Garzella, P. Breger, E. Mével, C. Dorrer, C. L. Blanc, F. Salin, and P. Agostini, Phys. Rev. Lett. **82**, 1668 (1999).
 - [11] E. A. Gibson, A. Paul, N. Wagner, R. Tobey, S. Backus, I. P. Christov, M. M. Murnane, and H. C. Kapteyn, Phys. Rev. Lett. **92**, 033001 (2004).
 - [12] L. A. Lompre, G. Mainfray, C. Manus, S. Repoux, and J. Thebault, Phys. Rev. Lett. **36**, 949 (1976).
 - [13] P. Lambropoulos, Phys. Rev. Lett. **55**, 2141 (1985).
 - [14] R. R. Freeman, P. H. Bucksbaum, H. Milchberg, S. Darack, D. Schumacher, and M. E. Geusic, Phys. Rev. Lett. **59**, 1092 (1987).
 - [15] F. Yergeau, S. L. Chin, and P. Lavigne, J. Phys. B **20**, 723 (1987).
 - [16] S. Augst, D. Strickland, D. D. Meyerhofer, S. L. Chin, and J. H. Eberly, Phys. Rev. Lett. **63**, 2212 (1989).
 - [17] P. B. Corkum, N. H. Burnett, and F. Brunel, Phys. Rev. Lett. **62**, 1259 (1989).
 - [18] E. Mevel, P. Breger, R. Trainham, G. Petite, P. Agostini, A. Migus, J.-P. Chambaret, and A. Antonetti, Phys. Rev. Lett. **70**, 406 (1993).
 - [19] U. Mohideen, M. H. Sher, H. W. K. Tom, G. D. Aumiller, O. R. Wood, R. R. Freeman, J. Boker, and P. H. Bucksbaum, Phys. Rev. Lett. **71**, 509 (1993).
 - [20] K. J. Schafer, B. Yang, L. F. Dimauro, and K. C. Kulander, Phys. Rev. Lett. **70**, 1599 (1993).

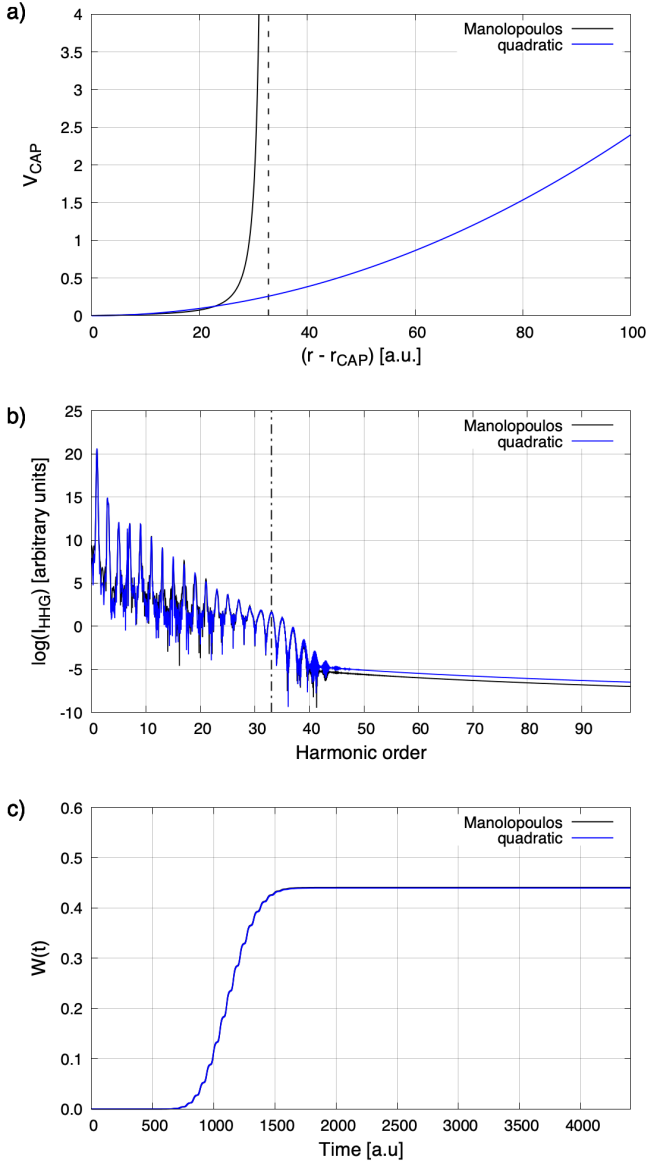


FIG. 4. a) Potential curves of the Manolopoulos CAP and the quadratic CAP employed in our calculations. The singular point of the Manolopoulos CAP is denoted with the dashed line. b) The HHG spectra of the hydrogen atom obtained with the Manolopoulos CAP and the quadratic CAP, at $I_0 = 2 \times 10^{14}$ W/cm² and $n_c = 20$. c) The time-resolved ionization probability of the hydrogen atom obtained with the Manolopoulos CAP and the quadratic CAP, at $I_0 = 2 \times 10^{14}$ W/cm² and $n_c = 20$.

[21] B. Walker, B. Sheehy, L. F. Dimauro, P. Agostini, K. J. Schafer, and K. C. Kulander, Phys. Rev. Lett. **73**, 1227 (1994).
 [22] J. B. Watson, A. Sanpera, D. G. Lappas, P. L. Knight, and K. Burnett, Phys. Rev. Lett. **78**, 1884 (1997).
 [23] R. Moshhammer, B. Feuerstein, W. Schmitt, A. Dorn, C. D. Schröter, J. Ullrich, H. Rottke, C. Trump, M. Wittmann, G. Korn, K. Hoffmann, and W. Sandner, Phys. Rev. Lett. **84**, 447 (2000).

[24] J. Muth-Böhm, A. Becker, and F. H. M. Faisal, Phys. Rev. Lett. **85**, 2280 (2000).
 [25] T. Weber, H. Giessen, M. Weckenbrock, G. Urbasch, A. Staudte, L. Spielberger, O. Jagutzki, V. Mergel, M. Vollmer, R. Dörner, and et al., Nature **405**, 658 (2000).
 [26] R. Taïeb, V. Vénier, and A. Maquet, Phys. Rev. Lett. **87**, 053002 (2001).
 [27] E. Gubbini, U. Eichmann, M. Kalashnikov, and W. Sandner, Phys. Rev. Lett. **94**, 053602 (2005).
 [28] P. Koval, F. Wilken, D. Bauer, and C. H. Keitel, Phys. Rev. Lett. **98**, 043904 (2007).
 [29] M. Busuladžić, A. Gazibegović-Busuladžić, D. B. Milošević, and W. Becker, Phys. Rev. Lett. **100**, 203003 (2008).
 [30] P. Eckle, A. N. Pfeiffer, C. Cirelli, A. Staudte, R. Dörner, H. G. Muller, M. Buttiker, and U. Keller, Science **322**, 1525 (2008).
 [31] A. L'Huillier, K. J. Schafer, and K. C. Kulander, Phys. Rev. Lett. **66**, 2200 (1991).
 [32] Z. Chang, A. Rundquist, H. Wang, M. M. Murnane, and H. C. Kapteyn, Phys. Rev. Lett. **79**, 2967 (1997).
 [33] C. Spielmann, N. H. Burnett, S. Sartania, R. Koppitsch, M. Schnürer, C. Kan, M. Lenzner, P. Wobrauschek, and F. Krausz, Science **278**, 661 (1997).
 [34] E. A. Gibson, A. Paul, N. Wagner, R. Tobey, D. Gaudiosi, S. Backus, I. P. Christov, A. Aquila, E. M. Gulikson, D. T. Attwood, M. M. Murnane, and H. C. Kapteyn, Science **302**, 95 (2003).
 [35] J. Seres, E. Seres, A. J. Verhoeve, G. Tempea, C. Streli, P. Wobrauschek, V. Yakovlev, A. Scrinzi, C. Spielmann, F. Krausz, and et al., Nature **433**, 596 (2005).
 [36] T. Popmintchev, M.-C. Chen, D. Popmintchev, P. Arpin, S. Brown, S. Alisauskas, G. Andriukaitis, T. Balciunas, O. D. Mücke, A. Pugzlys, and et al., Science **336**, 1287 (2012).
 [37] T. Brabec and F. Krausz, Rev. Mod. Phys. **72**, 545 (2000).
 [38] P. Salieres, T. Ditmire, K. S. Budil, M. D. Perry, and A. L'Huillier, J. Phys. B **27**, L217 (1994).
 [39] M. Bellini, C. Lyngå, A. Tozzi, M. B. Gaarde, T. W. Hänsch, A. L'Huillier, and C.-G. Wahlström, Phys. Rev. Lett. **81**, 297 (1998).
 [40] M. Chini, K. Zhao, and Z. Chang, Nat. Photonics **8**, 178 (2014).
 [41] F. H. M. Faisal, *Theory of multiphoton processes* (Plenum Press, 1987).
 [42] K. Amini, J. Biegert, F. Calegari, A. Chacón, M. F. Ciappina, A. Dauphin, D. K. Efimov, C. F. D. M. Faria, K. Giergiel, P. Gniewek, and et al., Rep. Prog. Phys. **82**, 116001 (2019).
 [43] A. Scrinzi, in *Attosecond and XUV Physics: Ultrafast Dynamics and Spectroscopy*, edited by T. Schultz and M. Vrakking (Wiley-VCH, Weinheim, 2014) pp. 257–292.
 [44] A. Nayak, M. Dumergue, S. Kühn, S. Mondal, T. Csizmadia, N. Harshitha, M. Füle, M. Upadhyay Kahaly, B. Farkas, B. Major, V. Szaszko-Bogár, P. Földi, S. Majorosi, N. Tsatrafyllis, E. Skantzakis, L. NeoričiĀĢ, M. Shirozhan, G. Vampa, K. Varjú, P. Tzallas, G. Sansone, D. Charalambidis, and S. Kahaly, Physics Reports **833**, 1 (2019).
 [45] C. F. de Morisson Faria and A. S. Maxwell, Reports on Progress in Physics **83**, 034401 (2020).

- [46] A. Jašarević, E. Hasović, R. Kopold, W. Becker, and D. B. Milošević, *Journal of Physics A: Mathematical and Theoretical* **53**, 125201 (2020).
- [47] J. Itatani, J. Levesque, D. Zeidler, H. Niikura, H. Pépin, J. C. Kieffer, P. B. Corkum, and D. M. Villeneuve, *Nature* **432**, 867 (2004).
- [48] C. I. Blaga, J. Xu, A. D. DiChiara, E. Sistrunk, K. Zhang, P. Agostini, T. A. Miller, L. F. DiMauro, and C. D. Lin, *Nature* **483**, 194 (2012).
- [49] K. C. Kulander, K. J. Schafer, and J. L. Krause, *Phys. Rev. Lett.* **66**, 2601 (1991).
- [50] J. L. Krause, K. J. Schafer, and K. C. Kulander, *Phys. Rev. A* **45**, 4998 (1992).
- [51] D. Bauer, *Phys. Rev. A* **56**, 3028 (1997).
- [52] J. Bauer, L. Plucinski, B. Piriaux, R. Potvliege, M. Gajda, and J. Krzywinski, *J. Phys. B* **34**, 2245 (2001).
- [53] M. Lein, N. Hay, R. Velotta, J. P. Marangos, and P. L. Knight, *Phys. Rev. A* **66**, 023805 (2002).
- [54] L.-Y. Peng and A. F. Starace, *J. Chem. Phys.* **125**, 154311 (2006).
- [55] C. Ruiz, L. Plaja, R. Taïeb, V. Vénier, and A. Maquet, *Phys. Rev. A* **73**, 063411 (2006).
- [56] E. A. Volkova, V. V. Gridchin, A. M. Popov, and O. V. Tikhonova, *J. Exp. Theor. Phys.* **102**, 40 (2006).
- [57] J. S. Prauzner-Bechcicki, K. Sacha, B. Eckhardt, and J. Zakrzewski, *Phys. Rev. Lett.* **98**, 203002 (2007).
- [58] E. A. Volkova, A. M. Popov, M. A. Tikhonov, and O. V. Tikhonova, *J. Exp. Theor. Phys.* **105**, 526 (2007).
- [59] A. D. Bandrauk, S. Chelkowski, D. J. Diestler, J. Manz, and K.-J. Yuan, *Phys. Rev. A* **79**, 023403 (2009).
- [60] A. M. Popov, M. A. Tikhonov, O. V. Tikhonova, and E. A. Volkova, *Laser Phys.* **19**, 191 (2009).
- [61] A. N. Grum-Grzhimailo, B. Abeln, K. Bartschat, D. Weflen, and T. Urness, *Phys. Rev. A* **81**, 043408 (2010).
- [62] S. Patchkovskii and H. G. Muller, *Comput. Phys. Commun.* **199**, 153 (2016).
- [63] A. D. Müller, E. Kutscher, A. N. Artemyev, L. S. Cederbaum, and P. V. Demekhin, *Chem. Phys.* **509**, 145 (2018).
- [64] E. S. Smyth, J. S. Parker, and K. Taylor, *Comput. Phys. Commun.* **114**, 1 (1998).
- [65] J. S. Parker, E. S. Smyth, and K. T. Taylor, *J. Phys. Bs* **31**, L571 (1998).
- [66] J. S. Parker, L. R. Moore, D. Dundas, and K. T. Taylor, *J. Phys. B* **33**, L691 (2000).
- [67] J. S. Parker, L. R. Moore, K. J. Meharg, D. Dundas, and K. T. Taylor, *J. Phys. B* **34**, L69 (2001).
- [68] J. S. Parker, B. J. S. Doherty, K. J. Meharg, and K. T. Taylor, *J. Phys. B* **36**, L393 (2003).
- [69] J. S. Parker, B. J. S. Doherty, K. T. Taylor, K. D. Schultz, C. I. Blaga, and L. F. Dimauro, *Phys. Rev. Lett.* **96**, 133001 (2006).
- [70] J. S. Parker, K. J. Meharg, G. A. McKenna, and K. T. Taylor, *J. Phys. B* **40**, 1729 (2007).
- [71] F. Robicheaux, *J. Phys. B* **45**, 135007 (2012).
- [72] K. C. Kulander, K. J. Schafer, and J. L. Krause, *Int. J. Quantum Chem.* **40**, 415 (1991).
- [73] K. C. Kulander, K. J. Schafer, and J. L. Krause, in *Atoms in intense laser fields*, edited by M. Gavrilu (Academic Press, Boston, 1992) pp. 247–300.
- [74] N. H. Shon, A. Suda, and K. Midorikawa, *Phys. Rev. A* **62**, 023801 (2000).
- [75] E. J. Takahashi, T. Kanai, K. L. Ishikawa, Y. Nabekawa, and K. Midorikawa, *Phys. Rev. Lett.* **99**, 053904 (2007).
- [76] M. Awasthi, S. Petretti, Y. V. Vanne, A. Saenz, A. Castro, and P. Decleva, *J. Phys. Conf. Ser.* **194**, 022064 (2009).
- [77] I. A. Ivanov and A. S. Kheifets, *J. Phys. B* **42**, 145601 (2009).
- [78] I. A. Ivanov and A. S. Kheifets, *Phys. Rev. A* **79**, 053827 (2009).
- [79] M. Abu-Samha and L. B. Madsen, *Phys. Rev. A* **81**, 033416 (2010).
- [80] S. Petretti, Y. V. Vanne, A. Saenz, A. Castro, and P. Decleva, *Phys. Rev. Lett.* **104**, 223001 (2010).
- [81] X.-M. Tong, G. Wachter, S. A. Sato, C. Lemell, K. Yabana, and J. Burgdörfer, *Phys. Rev. A* **92**, 043422 (2015).
- [82] C.-T. Le, V.-H. Hoang, L.-P. Tran, and V.-H. Le, *Phys. Rev. A* **97**, 043405 (2018).
- [83] M. Mandrysz, M. Kübel, J. Zakrzewski, and J. S. Prauzner-Bechcicki, *Phys. Rev. A* **100**, 063410 (2019).
- [84] A. Gordon, F. X. Kärtner, N. Rohringer, and R. Santra, *Phys. Rev. Lett.* **96**, 223902 (2006).
- [85] J. Javanainen, J. H. Eberly, and Q. Su, *Phys. Rev. A* **38**, 3430 (1988).
- [86] J. H. Eberly, Q. Su, and J. Javanainen, *Phys. Rev. Lett.* **62**, 881 (1989).
- [87] J. H. Eberly, Q. Su, and J. Javanainen, *J. Opt. Soc. Am. B* **6**, 1289 (1989).
- [88] Q. Su and J. H. Eberly, *J. Opt. Soc. Am. B* **7**, 564 (1990).
- [89] Q. Su and J. H. Eberly, *Phys. Rev. A* **44**, 5997 (1991).
- [90] R. Grobe and J. H. Eberly, *Phys. Rev. Lett.* **68**, 2905 (1992).
- [91] R. Grobe and J. H. Eberly, *Phys. Rev. A* **48**, 4664 (1993).
- [92] M. Lein, E. K. U. Gross, and V. Engel, *Phys. Rev. Lett.* **85**, 4707 (2000).
- [93] C. Ruiz, L. Plaja, L. Roso, and A. Becker, *Phys. Rev. Lett.* **96**, 053001 (2006).
- [94] A. Staudte, C. Ruiz, M. Schöffler, S. Schöessler, D. Zeidler, T. Weber, M. Meckel, D. M. Villeneuve, P. B. Corkum, A. Becker, and R. Dörner, *Phys. Rev. Lett.* **99**, 263002 (2007).
- [95] J. S. Prauzner-Bechcicki, K. Sacha, B. Eckhardt, and J. Zakrzewski, *Phys. Rev. A* **78**, 013419 (2008).
- [96] D. K. Efimov, A. Maksymov, J. S. Prauzner-Bechcicki, J. H. Thiede, B. Eckhardt, A. Chacón, M. Lewenstein, and J. Zakrzewski, *Phys. Rev. A* **98**, 013405 (2018).
- [97] C. Ruiz, L. Plaja, and L. Roso, *Phys. Rev. Lett.* **94**, 063002 (2005).
- [98] J. H. Thiede, B. Eckhardt, D. K. Efimov, J. S. Prauzner-Bechcicki, and J. Zakrzewski, *Phys. Rev. A* **98**, 031401 (2018).
- [99] D. K. Efimov, J. S. Prauzner-Bechcicki, J. H. Thiede, B. Eckhardt, and J. Zakrzewski, *Phys. Rev. A* **100**, 063408 (2019).
- [100] D. K. Efimov, J. S. Prauzner-Bechcicki, and J. Zakrzewski, *Phys. Rev. A* **101**, 063402 (2020).
- [101] K. Rzażewski, M. Lewenstein, and P. Salières, *Phys. Rev. A* **49**, 1196 (1994).
- [102] J. Chen, J. Liu, L. B. Fu, and W. M. Zheng, *Phys. Rev. A* **63**, 011404 (2000).
- [103] K. Sacha and B. Eckhardt, *Phys. Rev. A* **63**, 043414 (2001).

- [104] K. Sacha and B. Eckhardt, Phys. Rev. A **64**, 053401 (2001).
- [105] P. J. Ho, R. Panfili, S. L. Haan, and J. H. Eberly, Phys. Rev. Lett. **94**, 093002 (2005).
- [106] B. Eckhardt and K. Sacha, J. Phys. B: At. Mol. Opt. Phys. **39**, 3865 (2006).
- [107] F. Mauger, C. Chandre, and T. Uzer, Phys. Rev. Lett. **102**, 173002 (2009).
- [108] F. Mauger, C. Chandre, and T. Uzer, Phys. Rev. Lett. **105**, 083002 (2010).
- [109] J. Dubois, C. Chandre, and T. Uzer, Phys. Rev. Lett. **124**, 253203 (2020).
- [110] A. Kamor, F. Mauger, C. Chandre, and T. Uzer, Phys. Rev. Lett. **110**, 253002 (2013).
- [111] S. A. Berman, J. Dubois, C. Chandre, M. Perin, and T. Uzer, Phys. Rev. A **97**, 061402 (2018).
- [112] M. Kitzler, J. Zanghellini, C. Jungreuthmayer, M. Smits, A. Scrinzi, and T. Brabec, Phys. Rev. A **70**, 041401 (2004).
- [113] J. Caillat, J. Zanghellini, M. Kitzler, O. Koch, W. Kreuzer, and A. Scrinzi, Phys. Rev. A **71**, 012712 (2005).
- [114] X. Li, S. M. Smith, A. N. Markevitch, D. A. Romanov, R. J. Levis, and H. B. Schlegel, Phys. Chem. Chem. Phys. **7**, 233 (2005).
- [115] L. A. Nikolopoulos, T. K. Kjeldsen, and L. B. Madsen, Phys. Rev. A **76**, 033402 (2007).
- [116] M. Nest, T. Klamroth, and P. Saalfrank, Z. Phys. Chem. **224**, 569 (2010).
- [117] F. Ding, W. Liang, C. T. Chapman, C. M. Isborn, and X. Li, J. Chem. Phys. **135**, 164101 (2011).
- [118] P. Krause, T. Klamroth, and P. Saalfrank, J. Chem. Phys. **123**, 074105 (2005).
- [119] P. Krause, T. Klamroth, and P. Saalfrank, J. Chem. Phys. **127**, 034107 (2007).
- [120] L. Greenman, P. J. Ho, S. Pabst, E. Kamarchik, D. A. Mazziotti, and R. Santra, Phys. Rev. A **82**, 023406 (2010).
- [121] J. A. Sonk, M. Caricato, and H. B. Schlegel, J. Phys. Chem. A **115**, 4678–4690 (2011).
- [122] D. Hochstuhl and M. Bonitz, Phys. Rev. A **86**, 053424 (2012).
- [123] S. Bauch, L. K. Sørensen, and L. B. Madsen, Phys. Rev. A **90**, 062508 (2014).
- [124] P. J. Lestranger, M. R. Hoffmann, and X. Li, Adv. Quantum Chem. , 295 (2018).
- [125] X.-M. Tong and S.-I. Chu, Phys. Rev. A **57**, 452 (1998).
- [126] A. Castro, M. A. L. Marques, and A. Rubio, Journal. Chem. Phys. **121**, 3425 (2004).
- [127] K. Lopata and N. Govind, J. Chem. Theory Comput. **7**, 1344 (2011).
- [128] J. J. Goings, P. J. Lestranger, and X. Li, WIREs Comput. Mol. Sci. **8**, e1341 (2017).
- [129] M. Ruberti, V. Averbukh, and P. Decleva, J. Chem. Phys. **141**, 164126 (2014).
- [130] M. Ruberti, P. Decleva, and V. Averbukh, J. Chem. Theory Comput. **14**, 4991 (2018).
- [131] C. Huber and T. Klamroth, J. Chem. Phys. **134**, 054113 (2011).
- [132] S. Kvaal, J. Chem. Phys. **136**, 194109 (2012).
- [133] T. Sato, H. Pathak, Y. Orimo, and K. L. Ishikawa, J. Chem. Phys. **148**, 051101 (2018).
- [134] F. Jensen, WIREs Comput. Mol. Sci. **3**, 273 (2012).
- [135] M. Fiori and J. E. Miraglia, Comput. Phys. Commun. **183**, 2528 (2012).
- [136] M. S. Szczygieł, M. Lesiuk, and R. Moszyński, Theoretical description of the ionization processes with a discrete basis set representation of the electronic continuum (2019), arXiv:1909.07833 [physics.chem-ph].
- [137] K. Kaufmann, W. Baumeister, and M. Jungen, J. Phys. B **22**, 2223 (1989).
- [138] B. M. Nestmann and S. D. Peyerimhoff, J. Phys. B **23**, L773 (1990).
- [139] A. Faure, J. D. Gorfinkiel, L. A. Morgan, and J. Tennyson, Comput. Phys. Commun. **144**, 224 (2002).
- [140] B. I. Schneider, Phys. Rev. A **55**, 3417 (1997).
- [141] H. Bachau, E. Cormier, P. Decleva, J. E. Hansen, and F. Martín, Rep. Prog. Phys. **64**, 1815 (2001).
- [142] F. L. Yip, C. W. Mccurdy, and T. N. Rescigno, Phys. Rev. A **90**, 063421 (2014).
- [143] C. Marante, L. Argenti, and F. Martín, Phys. Rev. A **90**, 012506 (2014).
- [144] J. González-Vázquez, M. Klinker, C. Marante, L. Argenti, I. Corral, and F. Martín, J. Phys. Conf. Ser. **635**, 112110 (2015).
- [145] M. Labeye, F. Zapata, E. Coccia, V. Vénier, J. Toulouse, J. Caillat, R. Taïeb, and E. Luppi, J. Chem. Theory Comput. **14**, 5846 (2018).
- [146] E. Coccia, B. Mussard, M. Labeye, J. Caillat, R. Taïeb, J. Toulouse, and E. Luppi, Int. J. Quantum Chem. **116**, 1120 (2016).
- [147] E. Coccia and E. Luppi, Theor. Chem. Acc. **135**, 43 (2016).
- [148] E. Coccia, R. Assaraf, E. Luppi, and J. Toulouse, J. Chem. Phys. **147**, 014106 (2017).
- [149] E. Coccia and E. Luppi, Theor. Chem. Acc. **138**, 96 (2019).
- [150] E. Coccia, Mol. Phys. , 1 (2020).
- [151] T. H. Dunning, J. Chem. Phys. **90**, 1007 (1989).
- [152] W. Magnus, Commun. Pure Appl. Math. **7**, 649 (1954).
- [153] B. Klahn and W. A. Bingel, Int. J. Quantum Chem. **11**, 943 (1977).
- [154] M. Abramowitz and I. A. Stegun, *Handbook of mathematical functions with formulas, graphs, and mathematical tables* (Martino Publishing, 2014).
- [155] I. Cherkes, S. Klaiman, and N. Moiseyev, Int. J. Quantum Chem. **109**, 2996 (2009).
- [156] Y.-C. Han and L. B. Madsen, Phys. Rev. A **81**, 063430 (2010).
- [157] F. Johansson *et al.*, *mpmath: a Python library for arbitrary-precision floating-point arithmetic (version 1.1.0)* (2018), <http://mpmath.org/>.
- [158] J. Crank and P. Nicolson, Math. Proc. Camb. Philos. Soc. **43**, 50 (1947).
- [159] D. Bauer and P. Koval, Comput. Phys. Commun. **174**, 396 (2006).
- [160] V. Tulsy and D. Bauer, Comput. Phys. Commun. **251**, 107098 (2020).
- [161] R. Kosloff and D. Kosloff, J. Comput. Phys. **63**, 363 (1986).
- [162] U. V. Riss and H. Meyer, J. Chem. Phys. **105**, 1409 (1996).
- [163] D. E. Manolopoulos, J. Chem. Phys. **117**, 9552 (2002).
- [164] T. Gonzalez-Lezana, E. J. Rackham, and D. E. Manolopoulos, J. Chem. Phys. **120**, 2247 (2004).
- [165] T. P. Grozdanov and R. Mccarroll, J. Chem. Phys. **126**, 034310 (2007).
- [166] A. Ferré, A. E. Boguslavskiy, M. Dagan, V. Blanchet,

- B. D. Bruner, F. Burgy, A. Camper, D. Descamps, B. Fabre, N. Fedorov, and et al., *Nat. Commun.* **6**, 5952 (2015).
- [167] M. Matthews, F. Morales, A. Patas, A. Lindinger, J. Gateau, N. Berti, S. Hermelin, J. Kasparian, M. Richter, T. Bredtmann, O. Smirnova, J.-P. Wolf, and M. Ivanov, *Nat. Phys.* **14**, 695 (2018).
- [168] S. Pabst, A. Sytcheva, O. Geffert, and R. Santra, *Phys. Rev. A* **94**, 033421 (2016).
- [169] M. Ruberti, P. Decleva, and V. Averbukh, *Phys. Chem. Chem. Phys.* **20**, 8311 (2018).
- [170] P. Krause, J. A. Sonk, and H. B. Schlegel, *J. Chem. Phys.* **140**, 174113 (2014).
- [171] I. Y. Kostyukov and A. A. Golovanov, *Phys. Rev. A* **98**, 043407 (2018).
- [172] A. Sissay, P. Abanador, F. Mauger, M. Gaarde, K. J. Schafer, and K. Lopata, *J. Chem. Phys.* **145**, 094105 (2016).